



Inter-relationship between microstructure evolution and mechanical properties in inertia friction welded 8630 low-alloy steel

Amborish Banerjee¹ · Michail Ntovas¹ · Laurie Da Silva¹ · Salaheddin Rahimi¹ · Bradley Wynne^{1,2}

Received: 28 April 2021 / Revised: 23 August 2021 / Accepted: 2 September 2021 / Published online: 13 September 2021
© The Author(s) 2021

Abstract

The evolution of microstructure and mechanical properties in AISI 8630 low-alloy steel subjected to inertia friction welding (IFW) have been investigated. The effects of three critical process parameters, viz. rotational speed, friction and forge forces, during welding of tubular specimens were explored. The mechanical properties of these weld joints, including tensile and Charpy V-notch impact were studied for determining the optimum welding parameters. The weld joints exhibited higher yield strength, lower hardening capacity and ultimate tensile strength compared to base metal (BM). The maximum strength and ductility combination was achieved for the welds produced under a nominal weld speed of ~2900–3100 rpm, the highest friction force of ~680–720 kN, and the lowest axial forging load of ~560–600 kN. The measured hardness distribution depicted higher values for the weld zone (WZ) compared to the thermo-mechanically affected zone (TMAZ), heat-affected zone (HAZ) and BM, irrespective of the applied welding parameters. The substantial increase in the hardness of the WZ is due to the formation of microstructures that were dominated by martensite. The observed microstructural features, i.e. the fractions of martensite, bainite and ferrite, show that the temperature in the WZ and TMAZ was above A_{c3} , whereas that of the HAZ was below A_{c1} during the IFW. The fracture surface of the tensile and impact-tested specimens exhibited the presence of dimples nucleating from the voids, thus indicating a ductile failure. EBSD maps of the WZ revealed the formation of subgrains inside the prior austenite grains, indicating the occurrence of continuous dynamic recrystallisation during the weld. Analysis of crystallographic texture indicated that the austenite microstructure (i.e. FCC) in both the WZ and TMAZ undergoes simple shear deformation during IFW.

Keywords Inertia friction welding · Microstructure evolution · Welding parameters · Strain hardening · Crystallographic texture

1 Introduction

A key element for successful exploitation of newly discovered oil and gas fields in challenging geographical locations, both onshore and offshore, is transportation to depots by the aid of pipelines [1]. Considering the enormous difference in environmental conditions such as high pressures and

low temperatures throughout the transportation process, the application of high strength steels has been encouraged to avoid premature failures in service [2]. An excellent candidate material is AISI-8630, also designated as SAE-AISI 8630 (G8630) Ni–Cr–Mo steel owing to its optimal combination of strength and ductility over a wide temperature range. Currently, the most prevalent usage of AISI-8630 is structural components for subsea applications such as in oil extraction and transportation [3]. Other components include hangers, block valves and connectors for oil patch applications. The assessment of the structural integrity of pipe welds plays an essential part in the design of piping systems and quality assuring future performance in-service. The conventional fusion welding process results in a localised heterogeneity in the microstructure at the fusion zone, which makes the weld more susceptible to cracking and premature failure under extreme environmental conditions [4]. Hence,

✉ Amborish Banerjee
amborish.banerjee@strath.ac.uk;
amborishbanerjee1205@gmail.com

¹ Advanced Forming Research Centre (AFRC),
University of Strathclyde, 85 Inchinnan Drive,
Inchinnan, Renfrewshire 4 9LJ, PA, UK

² Department of Mechanical and Aerospace Engineering,
University of Strathclyde James Weir Building, 75 Montrose
Street, Glasgow G1 1XJ, UK

when optimising the process parameters, it is imperative to understand the extent of microstructure evolution during welding and establish structure–property correlations. Furthermore, it is equally important to identify the most efficient and economical welding method which can deliver superior mechanical properties.

Inertia friction welding (IFW) is a process variant of rotary friction welding (RFW) and among the solid-state joining processes used extensively for joining components with cylindrical or tubular cross sections [5]. During IFW, one side of the BM to be welded is coupled to the machine's flywheel, i.e. spindle, which is capable of accelerating the part to the desired angular velocity [6], whereas the other side is fixed on a bespoke fixture. Once the desired rotational speed is attained, the rotating workpiece is rubbed against the fixed work-piece, under an applied axial force, to generate frictional heat, resulting in the softening of the mating components at the interface and a solid-state joint [7]. The IFW process consists of three main stages: (1) the conditioning or the heating phase, where the friction between the rotating and stationary components leads to the generation of considerable heat and consequently an increase in the temperature of the weld interface, (2) the forging phase, where the heated materials are forged together axially under the rotary inertia forces leading to the joint and expulsion of the excess materials around the joint as flash, and (3) the post-IFW cooling stage, in which the axial force is maintained to consolidate the weld. There are several significant advantages of using IFW in comparison to the conventional fusion welding techniques. These include: (1) no requirement for filler material, shielding gas and welding flux during joining, (2) a significant reduction in solidification defects, e.g. porosity, cracking, and the absence of weld pool, (3) self-cleaning ability because of the wearing action of the rotating parts, (4) a comparatively narrower HAZ, (5) higher mechanical properties in the joint comparable to the BM, and (6) significantly lower levels of welding induced residual stress [6].

An extensive body of published literature exists on RFW covering different aspects of the welds, mechanical properties and microstructure evolution, including welding between dissimilar materials [8–11]. Dey et al. [8] reported welding between titanium and 304L stainless steel using continuous drive friction welding (CDFW) and evaluated the properties of the joints via tensile and bend tests. Failure was observed in the parent materials, signifying the superior qualities of the weld. The tensile and impact properties of inertia friction welded AISI 304 stainless steel was investigated by Sathiya et al. [9]. The increase in the friction time during IFW resulted in an inferior tensile strength compared to the BM. On the other hand, in terms of impact strength, the weld joint exhibited similar properties to that of the BM and the hardness increased with an increase in the friction time.

The authors also reported the formation of recrystallised grains in the weld zone (WZ) through continuous dynamic recrystallisation. Optimisation of the welding parameters, i.e. friction force, forging force, and rotation speed, was performed by Selvamani et al. [10] on AISI 1035 steel and the mechanical properties were evaluated. The IFW rotational speed was found to have a significant impact on the tensile strength, followed by forging and friction forces. In general, an increase in the rotational speed leads to noticeable thermal gradient and axial shortening (or upset) owing to the increase in the mass transfer from the weld interface. Hazra et al. [11] investigated the effect of forge force ranging from 20 to 60 kN on the mechanical properties and microstructure of nickel-free nitrogen steel and observed a decrease in the toughness of the welded joints compared to the BM with increased forge force. Additionally, the fracture surfaces of the failed specimens exhibited a ductile mode of failure due to the presence of dimples.

Despite the abundance of published literature on welding, it is notable that there is only limited information available on the RFW, especially IFW of AISI 8630 steel. To the knowledge of the authors, the effect of different process parameters on the mechanical properties of inertia friction welded AISI 8630 steel and the corresponding microstructure evolution has not been reported. The main aims of this study are to understand the effect of IFW process parameters, including rotational speed, friction and forge forces, on the mechanical properties of AISI 8630 steel, and to establish a correlation between microstructure features and the mechanical response of the weld, to determine the optimised welding conditions. Previous reports imply that analysing the evolution of crystallographic texture aids the determination of the dominant deformation mechanisms active during the welding process [12, 13]. For instance, Rahimi et al. [12] analysed the texture evolution during the friction stir welding of dissimilar steels (2205 duplex stainless steel to S275 low carbon–manganese steel) and reported the presence of dominant shear texture components. In another study on the texture evolution of microalloyed steel during friction stir welding, Rahimi et al. [13] observed a similar phenomenon. The authors reported dominant shear deformation in the austenite and ferrite phases of the weld material. Thus far, research works conducted on predicting the texture development of steels during RFW and understanding the predominant deformation modes are limited. Moreover, no detailed investigation of the texture evolution of AISI 8630 steel subjected to IFW has been documented in the literature. Thus, the texture evolution during IFW has also been studied and the major deformation modes have been identified.

Table 1 Nominal chemical composition of the as-received AISI 8630 steel

C	Cr	Mn	Ni	Mo	Si	Cu	Al	P	P	S	Fe
0.306	0.965	0.904	0.81	0.40	0.299	0.165	0.026	0.007	0.006	0.004	Bal

Table 2 Mechanical properties of the base metal

Yield strength (MPa)	Ultimate tensile strength (MPa)	Total elongation (%)	Hardness (HV)
588	751	28	~220

2 Experimental procedure

2.1 Material

Industrial-grade AISI 8630 steel, chemical composition shown in Table 1, was received in the form of 150 mm-long cylindrical tubes of inner and outer diameters of 50 and 80 mm, respectively. The as-received material was supplied in heat-treated condition that included (1) soaking the material at 860 °C for 3 h followed by water quenching, and (2) tempering at 680 °C for 5.30 h followed by air cooling. The mechanical properties of the as-received material are provided in Table 2.

2.2 IFW process

IFW was undertaken using a 125-ton MTI built RFW machine. The IFW process parameters matrix were restricted to three key parameters that have the most significant influence on weld microstructure, i.e. welding speed, friction and forge forces [14]. The Design of Experiments (DoE) was based on the Taguchi Orthogonal Array (ORA), specifically the L9 method [15], from which three parameters and three levels were selected. This method, combined with regression analysis, offers an organised, controlled and economic system for designing a range of optimised welding parameters. Note that the exact welding parameters used in this

study are subjected to proprietary information, and instead, a scaled range is provided for each case (see Table 3). Prior to the IFW, the mating faces of the cylindrical tubes were degreased with ethanol.

Figure 1a, b show a macrograph of a typical welded sample with the highlighted rotating end, fixed end and the flash generated during IFW, and a macrograph of the cross-sectional view of the weld, respectively. Flash is the excess material that is extruded during IFW from the weld interfaces. The TMAZ (refer Fig. 1c) is the region where the strain and temperature are comparatively lower than the WZ, and the HAZ is the area between the TMAZ and BM. Specimens for microstructure observations were taken from the weld joint, including the flash, and then mounted for metallography. Figure 1c shows a micrograph of a prepared and etched surface in which the different regions of the weld are highlighted and labelled.

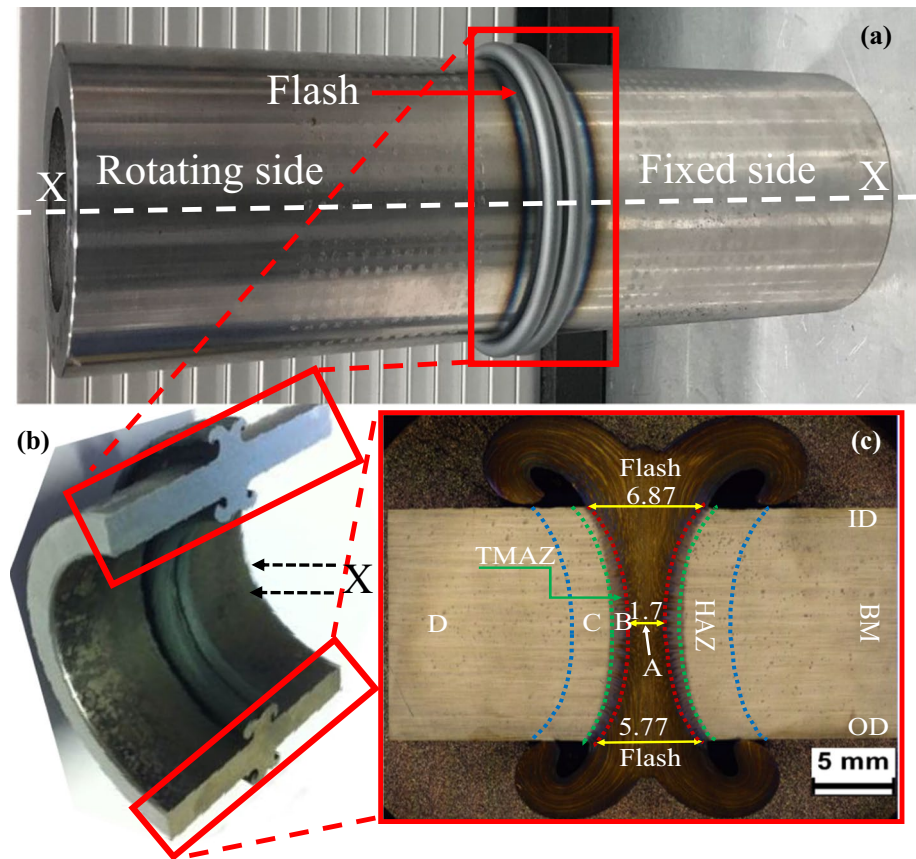
2.3 Microstructure characterisations

Metallographic samples were taken from the cross sections of the welds and then mechanically ground and polished to a mirror finished condition according to the ASTM E3-11 standard. The samples were then chemically etched with 2% nital solution to reveal the microstructure of the BM and different regions of the weld for microscopy observations. The prepared samples were examined using a Leica DM6000 M optical microscopy (OM) and FEI Quanta™ 250 field emission gun (FEG) scanning electron microscopy (SEM) equipped with a Nordlys II electron backscatter diffraction (EBSD) detector. For the EBSD analysis, the mirror-finished samples were further vibratory polished for 12 h using 0.05 µm colloidal silica suspension. The EBSD maps were collected with an accelerating voltage of 20 kV and 0.2 µm step size covering an area of 100 µm × 100 µm. In all cases,

Table 3 Welding parameters applied during the IFW process in this study

Specimen	Energy (KJ)	Weld speed (RPM)	Friction force (kN)	Forge force (kN)
IW1	525–550	2700–2900	560–600	560–600
IW2	525–550	2700–2900	620–660	620–660
IW3	525–550	2700–2900	680–720	680–720
IW4	600–625	2900–3100	560–600	620–660
IW5	600–625	2900–3100	620–660	680–720
IW6	600–625	2900–3100	680–720	560–600
IW7	650–675	3100–3300	560–600	680–720
IW8	650–675	3100–3300	620–660	560–600
IW9	650–675	3100–3300	680–720	620–660

Fig. 1 **a** A typical joint following IFW of the cylindrical tubes exhibiting rotating side, fixed side and the flash (not to scale), **b** cross-sectional [X–X cut in (a)] view of the weld joint, and **c** mounted specimen used for metallographic inspection (IW6 condition is presented in this case). The letters A, B, C and D (corresponding to the WZ, TMAZ, HAZ and BM, respectively) in (c) represent the locations of the EBSD scans shown in Fig. 4. All dimensions in **c** are in mm



a minimum of 77% of the scanned areas were indexed. The post-processing of the obtained data was performed using HKL-channel 5 software. Moreover, to understand the evolution of texture and to determine the dominant deformation mechanisms during IFW, further analyses were carried out on the acquired EBSD maps for each region by reconstructing prior austenite grains using MTEX tool in MATLAB according to Kurdjumov–Sachs orientation relationship based on a method described by Nyssosen et al. [16].

2.4 Mechanical testing

Microhardness measurements across different regions of the weld were carried out on the sample cross sections using a Struers Vickers microhardness testing machine by applying a 200 gf (1.96 N) load over 12 s dwell time. In total, ~500–550 measurements were performed to construct a reliable hardness map for all nine welded specimens, with 0.3 mm spacing in X and 1 mm spacing in Y directions between indentations.

Quasi-static tensile tests at ambient condition were performed according to the ASTM E-8 M standard [17] on tensile specimens with a gauge diameter and a length of 6 mm and 30 mm, respectively. The experiments were carried out using a Zwick Z250/SW5A screw-driven tensile testing machine

equipped with a load cell of 250 kN. The tests were performed under a constant strain rate of 2.5×10^{-4} 1/s where the strain was measured using an extensometer of 20 mm gauge length. For each welding condition, three tests were conducted to ensure repeatability in the results. The strength and ductility of the welded specimens were evaluated, and the hardening capacity and the strain-hardening behaviour were analysed.

Charpy V-notch (CVN) impact tests were also performed on the specimens according to the ASTM-370 standard [18] at sub-zero (-46 °C) temperature to assess and evaluate the impact toughness of the welds. Owing to the geometrical constraints of the welded specimens, sub-sized samples of 55 mm \times 10 mm \times 2.5 mm were manufactured for these tests. Moreover, the fracture surfaces of both tensile and impact specimens were examined by the SEM to analyse the failure mechanisms and to compare them with associated microstructure.

3 Results

3.1 Microstructure of the BM

Figure 2a shows the SEM micrograph of the BM exhibiting the presence of multiple bainite morphologies. These

include plate-like bainite (PLB), granular bainite (GB), upper bainite (UB), and lower bainite (LB). Typically, PLB is characterised by the presence of carbide precipitates inside the irregular ferritic structure, whereas GB is carbide free [27]. Moreover, the presence of both UB and LB is noticed in the BM microstructure as highlighted in Fig. 2a. Previous report on other microalloyed steels shows that in the UB, the carbide precipitates are predominantly observed at the lath boundaries, whereas in the LB, they were inside the laths [19].

The orientation image map (OIM) of the BM with inverse pole figure (IPF) colouring with respect to the axial direction (AD) is shown in Fig. 2b. The microstructure exhibited elongated and coarse grains in addition to the typical lath/plate-like morphology. There was also some heterogeneity observed in the grain size ranging from 0.2 to 23.6 μm . No strong texture was observed in the BM as can be observed in Fig. 2c in the form of $\{100\}$, $\{110\}$ and $\{111\}$ pole figures.

3.2 Microstructure evolution during IFW

Figure 3 shows the OM and SEM micrographs obtained from different regions of the IW6 weld (the optimum weld

condition) highlighted in Fig. 1c. The weld shows the three well-observed friction welded zones: WZ, TMAZ and the HAZ. The microstructure of the WZ (refer Fig. 3a) is dominated by martensite ($\approx 80\%$) with bainite ($\approx 15\%$) and retained austenite (RA, $\approx 5\%$) also being observed. The OM micrograph of the etched WZ shown in Fig. 3b further confirms the much lower fractions of bainite and RA on the bulk scale, owing to their brighter appearance (indicated by arrows). This martensite observation indicates the WZ material has exceeded A_{c3} temperature, i.e. the material was fully austenitic and the cooling rate was rapid, most likely because of BM acting as a heat sink. Additionally, the formation of lath type bainitic-ferrite (BF) sheaves is observed in the WZ surrounded by martensite (see Fig. 3a). These BF sheaves are reported by Bhadeshia et al. [20] to be made up of both UB and LB plates, which are separated by martensite, RA or cementite. The microstructure of the TMAZ (Fig. 3c) shows a uniform distribution of all the present phases including martensite, bainite and ferrite. Moreover, an increase in the presence of rod-shaped carbide precipitates was also observed in Fig. 3c, highlighted by circles. The HAZ (Fig. 3d) has a microstructure similar to the BM, indicating that its temperature did not exceed the A_{c1} temperature. In

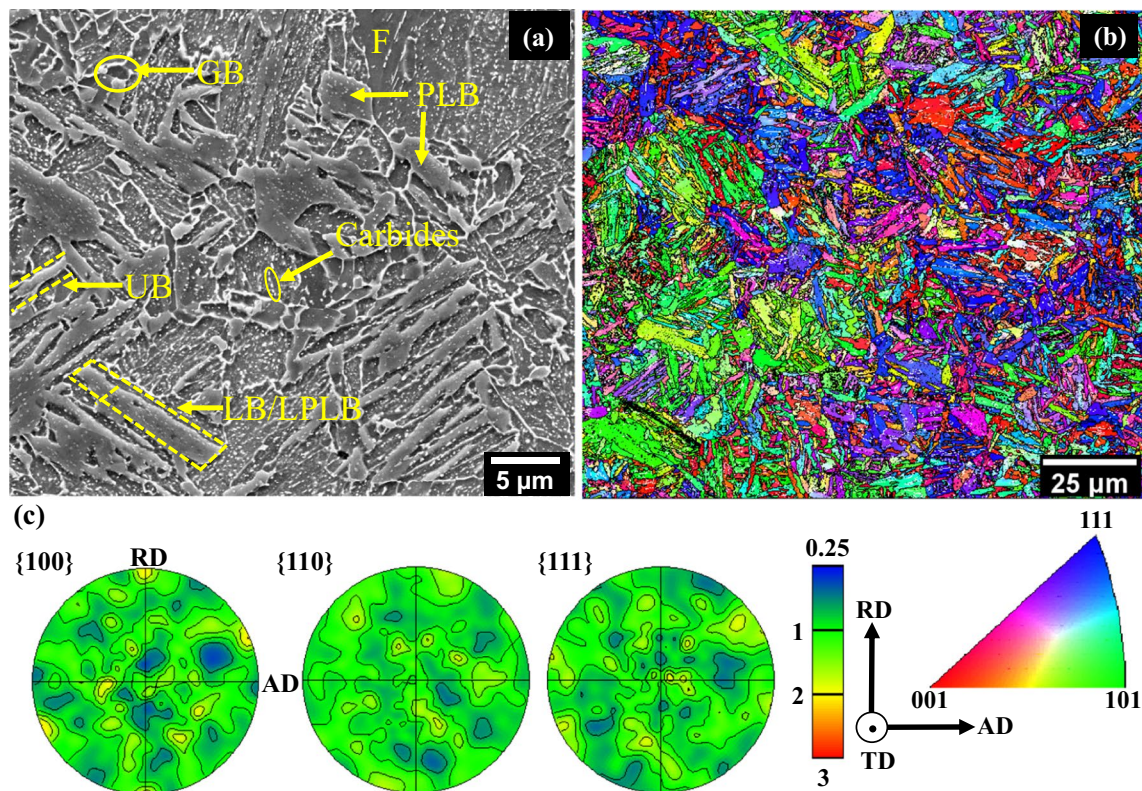
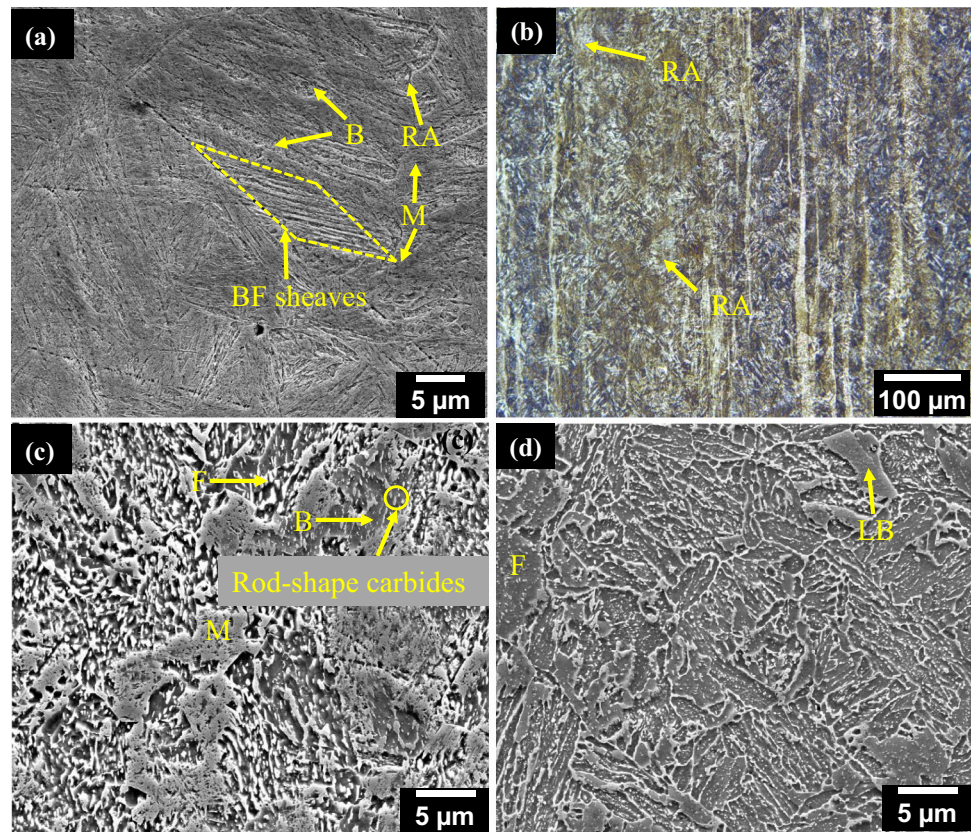


Fig. 2 Microstructure characteristics of the BM; **a** SEM image exhibiting the presence of granular bainite, plate-like bainite (PLB), upper and lower bainite (UB and LB), ferrite (F) and carbide precipitates, **b** OIM with IPF colouring with respect to AD, and **c** $\{100\}$, $\{110\}$ and

$\{111\}$ pole figures depicting the initial texture in the BM. The terms AD, RD and TD refer to the axial, radial and tangential directions, respectively

Fig. 3 Micrographs obtained from the different regions of IW6 weld; **a** SEM image of WZ exhibiting the presence of BF sheaves, martensite and RA, **b** OM image of the WZ confirming the presence of predominant martensite along with bainite and RA, **c** SEM image of the TMAZ indicating the existence of ferrite, martensite and bainite, and **d** SEM image of the HAZ exhibiting a microstructure similar to that of the BM



turn, the temperature within the TMAZ must have been near or above A_{c3} , and the presence of ferrite and bainite along with martensite is due to the slower cooling rate. These conclusions have been supported by the texture analyses and are discussed in detail in Sect. 4.2.

The OIMs of different regions of the IW6 weld with IPF colouring with respect to the axial direction (AD) and their grain size distributions are shown in Fig. 4. As previously stated, the BM was found to have a predominantly lath structure with sizes ranging from 0.2 to 23.6 μm . In comparison, the martensite and bainite lath size in the WZ was much more refined, in the size range of 0.2–12.2 μm , and the microstructure packets were equiaxed. This suggests continuous dynamic recrystallisation of the austenite during IFW leading to a microstructure with fine grain size, which upon cooling confines the martensite packets within the small austenite grains such that there appears to be only one packet per grain. This has been shown by reconstructing prior austenite grains in the EBSD map (Fig. 12b) where the majority of packets appear to have originated from individual austenite grains. Even in the TMAZ where the temperature was slightly lower than that of the WZ but still at or above the A_{c3} , full transformation to austenite occurred. However, in comparison to the WZ, significant austenite grain growth has occurred in TMAZ that might be due to the lower level of shear deformation. Therefore, instead of the

equiaxed grains, elongated laths with sizes varying from 0.2 to 27.8 μm were formed from the austenitic microstructure with large grain size on cooling at a relatively slower cooling rate than that of the WZ. In the HAZ, the grain size ranged from 0.2 to 27.5 μm , which was very similar to that of the BM. This argument is further strengthened by the plots of misorientation angle distributions for the different regions of the weld and the BM, shown in Fig. 5. In comparison to the TMAZ, HAZ and BM, the WZ shows a much lower number of boundaries with 50–60 degrees misorientation, i.e. where boundaries between individual martensite packets from the same parent austenite grain exist [21]. This again confirms that the martensite and bainite packets are confined within the small dynamically recrystallised austenite grains and the small size of the grains did not allow the formation of different martensite variants within the same grain. Interestingly, this means that the small austenite grain size reduces the total number of HAGBs in the WZ in comparison to the other zones.

The $\{100\}$, $\{110\}$ and $\{111\}$ pole figures of the WZ, TMAZ and HAZ, plotted from the OIMs in the sample reference frame across the weld zones, are shown in Fig. 4g, h and i. The textures are relatively weak, but there is a clear rotated transformed shear texture in both the WZ and TMAZ, confirming that deformation is dominated by shear in these regions.

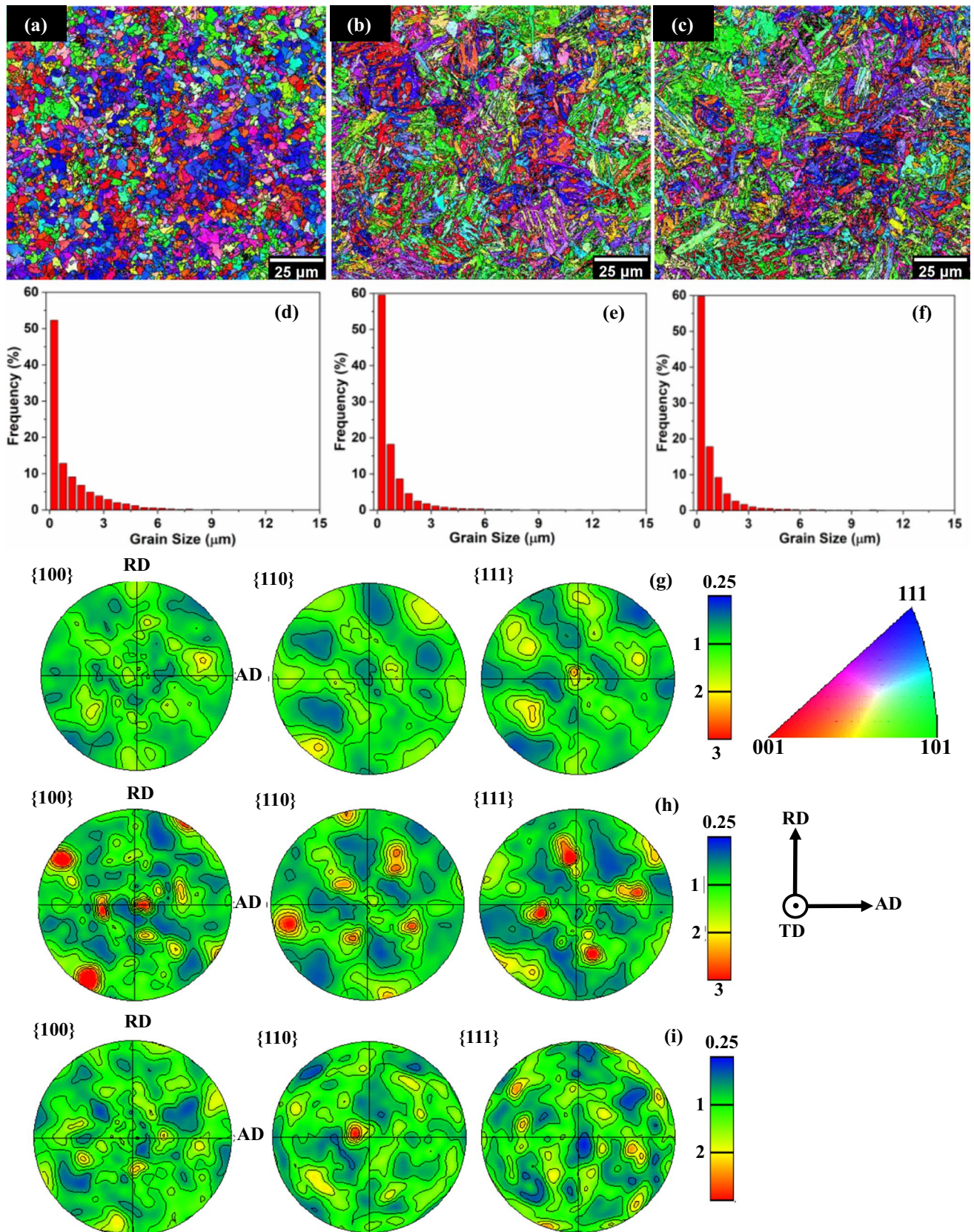
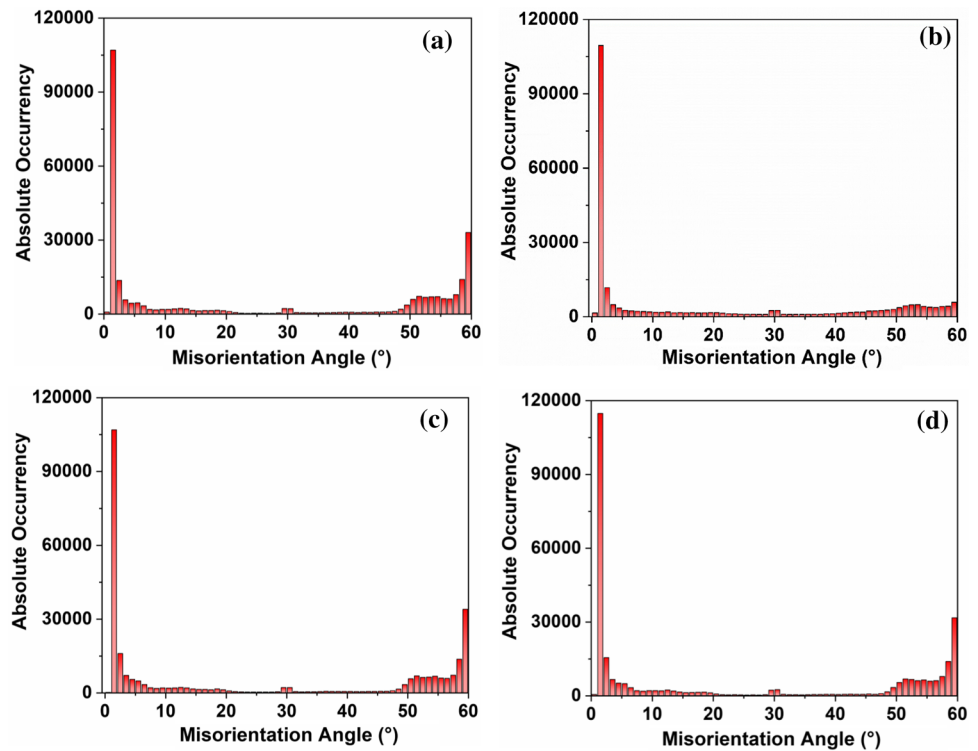


Fig. 4 OIMs with IPF colouring with respect to the AD, and grain size distributions for different regions of the IW6 weld, **a, d** WZ, **b, e** TMAZ, **c, f** HAZ. {100}, {110} and {111} pole figures showing the post-IFW textures in the **g** WZ, **h** TMAZ, and **i** HAZ

Fig. 5 Misorientation angle distributions of the **a** BM, **b** WZ, **c** TMAZ and **d** HAZ of the IW6 specimen. The scan area and the step size for all the EBSD maps were identical, i.e. $100 \times 100 \mu\text{m}^2$ and $0.2 \mu\text{m}$, respectively



3.3 Weld microhardness

Fig. 6 shows the microhardness map for the weld produced under IW6, i.e. the optimum condition, along with hardness profiles across three lines at different locations, covering all zones of the weld. The maximum hardness (refer Fig. 6a) was measured in the WZ (~684 HV), which exhibited a predominantly martensitic structure. On the other hand, the hardness measured in the BM was the lowest (~220–230 HV). The hardness profiles of the different

zones, i.e. TMAZ and HAZ, showed a decreasing trend on moving away from the WZ towards the BM. This distribution was found to be similar, if not identical, for the rest of the welded specimens. Additionally, a variation in the average microhardness values was also recorded at the top (inner diameter), middle (centre line) and bottom (outer diameter) locations of the WZ (Fig. 6b). Overall, a significant variation in the hardness distribution was measured across different regions of the weld when moving from one side to the other through HAZ, TMAZ and WZ.

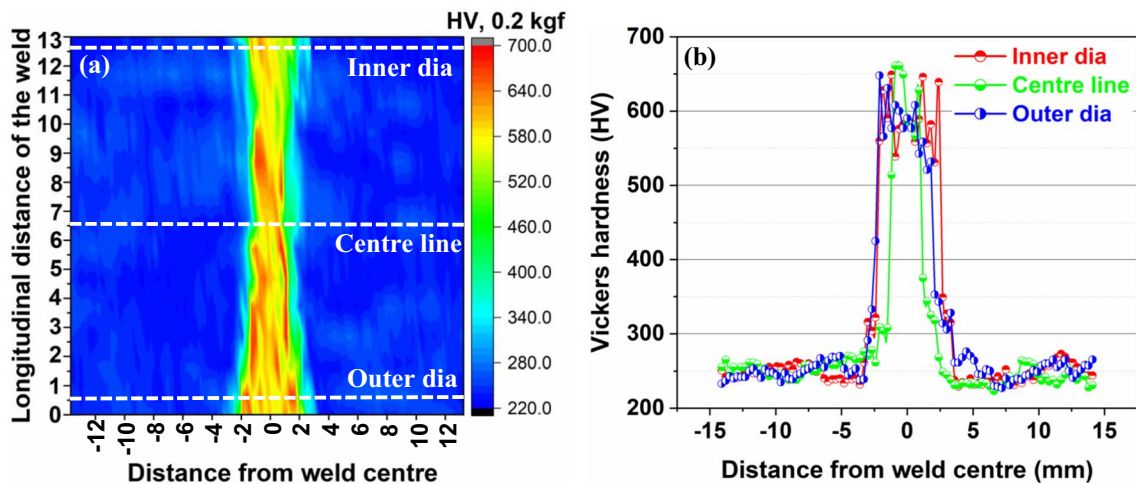


Fig. 6 **a** Microhardness map of the weld cross section produced under IW6 condition, including the BM, HAZ, TMAZ and WZ, and **b** microhardness profiles along the lines shown in (a)

3.4 Weld mechanical properties

The results of tensile tests conducted under a constant 2.5×10^{-4} 1/s strain rate, in the form of engineering stress–strain curves, for the welded specimens are presented in Fig. 7a. For the majority of the tests, the final fracture was observed to occur between the HAZ and the BM. As is evident from the inset in Fig. 7a, the samples exhibited discontinuous yielding and a significant variation in the upper and the lower yield point.

The yield (σ_y) and the UTS values along with the error bars calculated as the standard error of three tests for the weld specimens are shown in Fig. 7b and c, respectively. The yield and UTS of the BM were measured to be ≈ 588 MPa and 751 MPa, respectively. The stress–strain curve and the strain-hardening behaviour of the BM, which is strain-rate insensitive, are provided in the supplementary information (SD). In comparison to the BM, all the weld specimens exhibited an overall increase in the yield strength. In terms of UTS, all the weld specimens (except that of the IW6 condition) exhibited a decrease in the UTS.

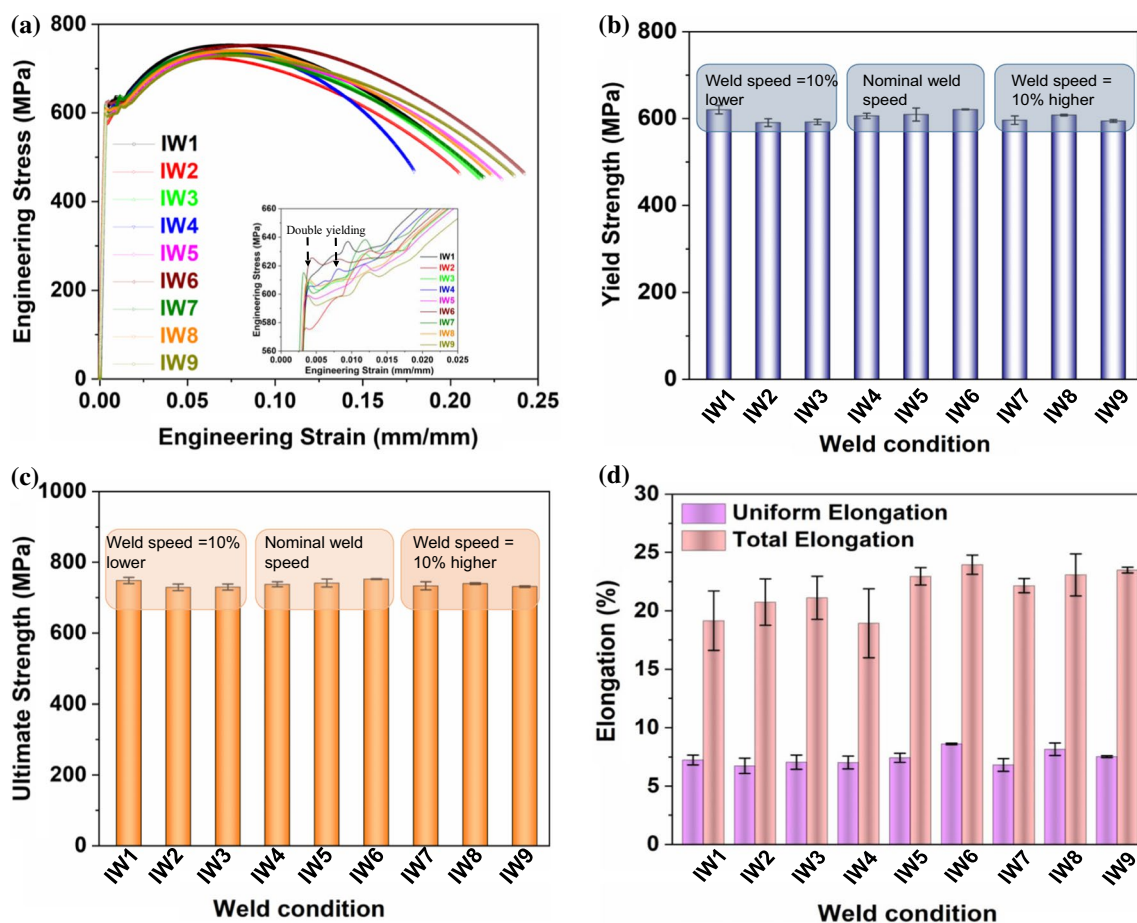


Fig. 7 The tensile properties measured for the welded materials after IFW including **a** engineering stress–strain curves, **b** yield strength, **c** UTS, and **d** uniform and total elongations, all obtained from the stress–strain curves shown in (a)

The IW6 was a welding condition under which a nominal weld speed of 1950–2050 rpm, highest frictional force of 680–720 kN, and lowest forge force of 560–600 kN were applied during IFW (refer Table 3). This condition led to the highest measured yield stress, and the highest static toughness of ~ 161 MJ/m³ (Fig. 9). Thus, these data show that higher frictional forces and lower forge forces lead to the optimum yield strength and ductility in the weld material. In terms of total elongation (Fig. 7d), an upsurge was measured with an increase in the friction force. All the welded specimens exhibited an adequate level of strain hardening followed by strain localisation in the form of necking and final fractures (Fig. 11).

To investigate the strain-hardening behaviour of the as-welded materials, the hardening capacity (H_c) and strain-hardening exponent (n) were evaluated for the plastic regime of the measured stress–strain curves. The hardening capacity is defined as the ratio of the UTS to the yield strength which was later redefined by Afrin et al. [22] through a normalised relationship presented in Eq. 1.

$$H_c = \frac{\sigma_u}{\sigma_y} - 1 \tag{1}$$

In Eq. 1, σ_u and σ_y are the UTS and the yield strength, respectively. The evaluated hardening capacity of the welded specimens is presented in Fig. 8a. As shown, an overall decrease in the hardening capacity for the welded materials was calculated, compared to the ≈ 0.28 of the BM (provided in the SD).

For understanding the strain-hardening (or softening) behaviours of the welded materials and the BM, the strain-hardening exponent (n), expressed by the Hollomon equation (see Eq. 2) [23], was evaluated from the plastic deformation regimes of the stress–strain curves measured for these conditions.

$$\sigma = K\varepsilon^n. \tag{2}$$

In Eq. 2, σ and ε represent the true stress and true plastic strain, respectively, K is the coefficient of strength, and n is the strain-hardening exponent (SHE). The log–log plots of the true stress–true plastic strain are shown in Fig. 8b for all welds and the BM and their corresponding strain-hardening exponent values are presented in Table 4. The initial peaks in the $\ln \sigma$ – $\ln \varepsilon$ curves (Fig. 8b) are due to the double-yielding phenomena. These initial peaks were excluded from the calculation of the strain-hardening

coefficients for the welded materials, and only the uniform sections were considered. The logarithmic true stress–true strain curves (i.e. $\ln \sigma$ – $\ln \varepsilon$) shown in Fig. 8b exhibited dual-slope inclinations which signifies two stages of strain-hardening behaviours. These are represented by n_1 and n_2 for the lower regime, also termed as the first stage, and the upper regime, the second stage, respectively. The values calculated for n_1 and n_2 were in the ranges of 0.158–0.174 and 0.083–0.105, respectively. Those measured for the BM were ≈ 0.336 and ≈ 0.187 , respectively (refer to SD). This indicates an almost two times decrease in the work-hardening behaviours of the welded materials in both the upper and lower regimes.

The static toughness, i.e. the area under the stress–strain curve, was calculated for all the IFW conditions and is shown in Fig. 9. Static toughness is a measure of the energy-absorbing capacity of the material prior to failure. As shown in Fig. 9, a combination of higher rotational speed and friction force during IFW (i.e. those of IW5, 6, 8 and 9) leads to a higher static toughness. In general, material with the highest static toughness exhibits the optimum combination of strength and ductility. Thus, based on the calculated static toughness, IW6 is the optimum IFW condition for the materials among those investigated in this study.

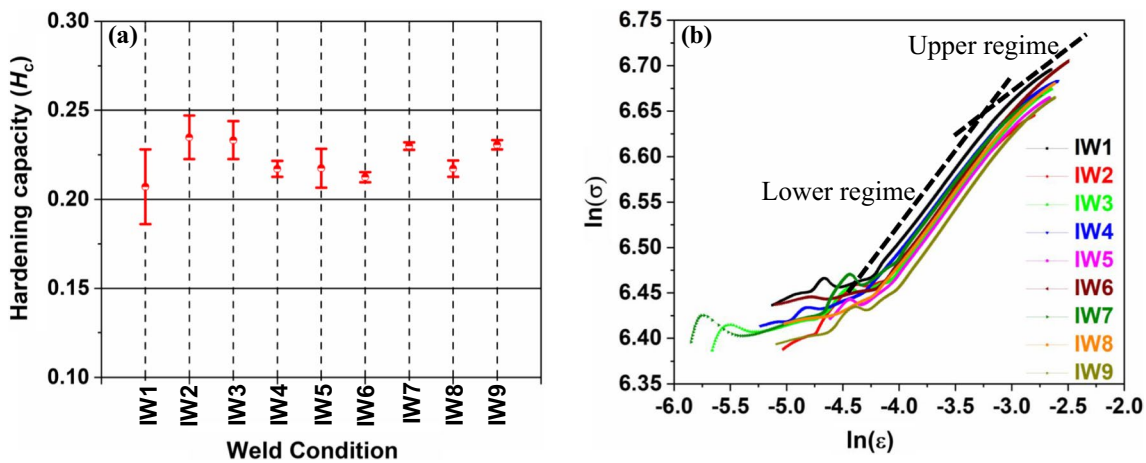


Fig. 8 a Hardening capacity evaluated for the BM and the welded materials, and b logarithmic true stress–true strain curves for the BM and all the welded specimens exhibiting strain-hardening behaviours

based on the Hollomon relationship in Eq. 2. The bold broken black lines highlight the change in the inclinations of the curves

Table 4 The evaluated strain-hardening exponents (n) for the BM and all the welded materials. n_1 and n_2 represent the first and secondary slopes measured for each condition

Condition	BM	IW1	IW2	IW3	IW4	IW5	IW6	IW7	IW8	IW9
n_1	0.336	0.162	0.161	0.169	0.159	0.169	0.171	0.164	0.163	0.174
n_2	0.187	0.097	0.093	0.101	0.083	0.094	0.104	0.096	0.105	0.104

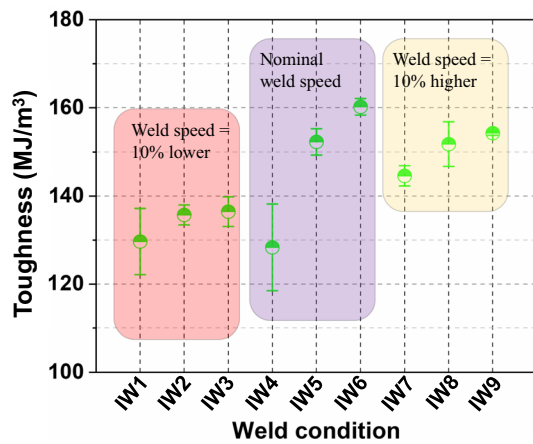


Fig. 9 The calculated static toughness values for the BM and the welded materials

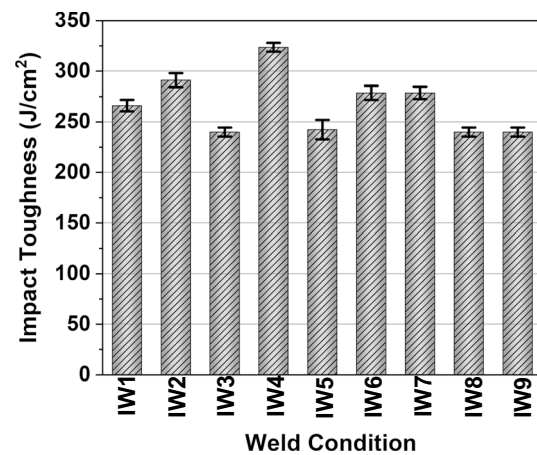


Fig. 10 Results of Charpy impact tests conducted on the BM and the welded materials at $-46\text{ }^{\circ}\text{C}$

3.5 Charpy impact tests

The results of the Charpy impact tests obtained for the sub-sized specimens (i.e. $55\text{ mm} \times 5\text{ mm} \times 2.5\text{ mm}$), imposed by the geometry of the welded specimens, were proportionally converted to values corresponding to the standard size samples (i.e. $55\text{ mm} \times 10\text{ mm} \times 10\text{ mm}$), based on the approach documented by Wallin et al. [24]. The impact toughness values obtained from the sub-sized specimens are presented in Table 5, and the converted values are presented in Fig. 10. As can be observed from the graph, all the tested specimens exhibited impact toughness in the range of $240\text{--}323.5\text{ J/cm}^2$, where the highest impact toughness was recorded for the IW4 specimen ($\sim 323.5\text{ J/cm}^2$). In general, with a decrease in the plastic deformation capacity of the material, the impact toughness displays an increasing trend. The reported results in Fig. 10 are in good agreement with the strain-hardening behaviour presented in Fig. 8b in which the lowest n value, i.e. the ability of plastic deformation before the onset of plastic instability, was calculated for the IW4 condition. The fracture morphology of the Charpy impacted specimens exhibited a dull appearance with a fibrous zone which is an indication of a ductile failure of the welded specimens.

3.6 Fracture surface analysis

The fracture surfaces of the specimens made under IW6 welding condition, following both tensile and Charpy

impact tests, were examined by SEM to understand the deformation and fracture behaviours. Figure 11a shows a micrograph of the post-tensile fracture surface depicting cup–cone fracture (refer to the insert in Fig. 11a) with a dull and fibrous appearance. As stated earlier, final failures in the tensile specimens predominantly occurred in a region between the HAZ and the BM. The micrographs in Fig. 11a exhibit the presence of mostly equiaxed dimples, which is an indication of ductile failure. The higher magnification micrograph shown in Fig. 11b reveals the initiation of these dimples from microvoids, which are uniformly distributed over the central regions of the tensile specimen’s cross section. Figure 11c shows a micrograph taken from the edge of the fracture surface. A higher magnification micrograph of this region, shown in Fig. 11d, provides evidence of the presence of parabolic dimples in addition to equiaxed dimples. The presence of these elongated parabolic dimples (see Fig. 11d) is an indication of shear deformation during the uniaxial tensile test.

Micrographs of the fracture surface of the IW6 specimen following the Charpy impact test are shown in Fig. 11e, f. The fracture surface exhibits protruding shear lips on both sides (see Fig. 11e), which is an indication of the ductile behaviour of the material. The high magnification micrograph (see Fig. 11f) shows dimples similar to those observed on the post-tensile fracture surface (see Fig. 11b); however, fewer microvoids were observed. Furthermore, all the welded specimens (i.e. IW1–IW9) exhibited a similar fracture morphology.

Table 5 The impact toughness of all the welded materials carried out on sub-sized specimens

Condition	IW1	IW2	IW3	IW4	IW5	IW6	IW7	IW8	IW9
Impact toughness (J/cm^2)	266.1	291.2	240.0	323.5	242.3	278.6	278.6	240.0	240.0

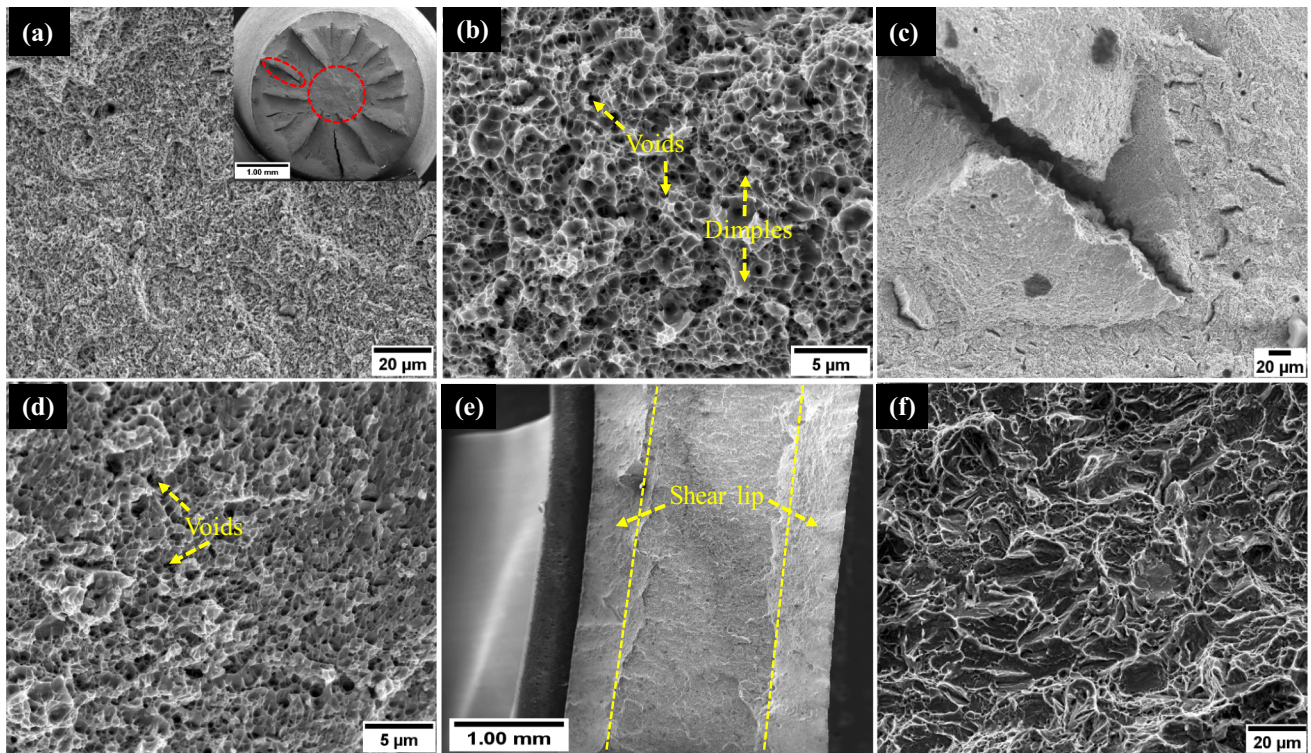


Fig. 11 SEM micrographs of the fracture surfaces of **a–d** tensile, and **e–f** Charpy impact tests, on IW6 specimen. **a** Dimples in the central region of the cross section and the cup–cone fracture in the inset, **b** a magnified micrograph demonstrating the presence of microvoids and

their coalescence to form equiaxed dimples, **c** an edge crack, **d** presence of elongated and equiaxed dimples, **e** overall fracture surface after Charpy impact test exhibiting shear lips, and **f** dimples on the fracture surface of the impacted specimen

4 Discussion

4.1 Microstructure evolution during IFW

In the optical macrograph presented in Fig. 1c, the weld region can clearly be observed in the BM. However, different zones of the weld, i.e. TMAZ and HAZ, cannot be distinguished. The differences in the microstructure features across the various weld zones were only observed at higher magnifications (see Fig. 3). No direct measurements of temperature were conducted on the weld during IFW; thus, based on the observed microstructures on the weld cross section, the likely temperatures experienced by the material can be estimated. The Ac_1 and Ac_3 temperatures of the investigated material were calculated to be $\approx 730 \pm 20$ °C and 772 ± 15 °C, respectively, based on the nominal chemical composition (see Table 1), according to Eqs. (3) and (4) [25].

$$Ac_1 = 727 - (10.7Mn) - (16.9Ni) + (29.1Si) + (16.9Cr) + (6.38W) + (290As), \quad (3)$$

$$Ac_3 = 910 - (203\sqrt{C}) + (30Mo) + (44.7Si) + (15.2Ni) + (31.5Mo) + (97V). \quad (4)$$

Similarly, the martensite start and finish temperatures, i.e. M_s and M_f , respectively, were assessed to be 325 and 209 °C. On this rationale, it can be inferred that the temperature in the WZ and TMAZ were at or above the Ac_3 temperature ($\approx 772 \pm 15$ °C) owing to the existence of predominantly martensitic and bainitic microstructure. The HAZ experienced temperatures below the Ac_1 ($\approx 730 \pm 20$ °C) temperature and, as a result, no phase transformation occurred. Similar conclusions have been made by Baker et al. [26] on correlating the evolution of microstructure in microalloyed steel to the likely temperature profiles during friction stir welding.

The heat generated during the conditioning phase of the IFW aids the faying surfaces of the rotating and fixed components to attain a temperature above Ac_3 ($\approx 730 \pm 20$ °C). This leads to the predominant transformation of the BM microstructure in the WZ and TMAZ to austenite. The austenite phase is then subjected to severe shear deformation during the ongoing IFW process that is likely to result in continuous

dynamic recrystallisation in the austenite, which then transforms to martensite, bainite and ferrite upon cooling depending on the heat exchange rate with the BM and the environment. This is however not the case in the HAZ, due to lower temperatures and absence of enough shear strain, as a result of which the microstructure is similar to that of the BM. It is understood that the application of high levels of strain to austenitic microstructure at an appropriate temperature followed by rapid undercooling results in the formation of ferrite in the austenite matrix [27].

Since the WZ experienced temperatures at or above A_{c3} during the initial stage of the IFW process, the majority of the microstructure must have been transformed to austenite just before the start of the second stage of welding. Once the second stage of IFW was initiated and severe shear deformation applied, strain-induced dynamic recrystallisation had occurred in the austenite phase leading to the formation of small grains with significantly higher fractions of grain boundaries and triple junctions that are favourable sites for the nucleation of martensite on cooling during the final stage of the IFW. The size of the prior austenite grains (PAGs) in the WZ ranged from 4 to 21 μm and its average grain size was calculated to be $\sim 11 \mu\text{m}$ (refer Fig. 12). These small dynamically recrystallised PAGs in the WZ transformed to small martensite colonies of size ranging from 0.2 to 12.2 μm (see Figs. 3b, 4d) on cooling from welding temperature such that they appeared as equiaxed grains in the EBSD map (Fig. 4a).

Casero et al. [28] reported the significance of prior austenite grain size on the transformation to martensite. The authors concluded that the refinement of the austenite grains resulted in a decrease in the M_s temperature and an increase in the austenite to martensite transformation owing to the continuous formation of the martensitic laths. Moreover, it

is equally important to comprehend the influence of austenitisation conditions as it results in the prior austenite grain structure, which in turn determines the formation and morphology of lath martensite. In a transformed microstructure, martensite is present in different forms consisting of packets, blocks and laths [29]. As shown schematically in Fig. 12a, martensite grains nucleate on triple junctions and grain boundaries of the prior austenite grains and form packets having different $\gamma//\alpha$ parallel planes (i.e. different variants of the prior austenite) and with HAGB between them. These packets are further subdivided into numerous blocks with high angle misorientation relationship. The block consists of lath martensite consisting of numerous subgrains [30]. The EBSD maps of the WZ presented in Fig. 4a show very small martensite packet size such that the martensite grains appear as equiaxed grains. This is because the packets are confined between the small prior austenite grains in the WZ that were dynamically recrystallised during IFW. Figure 12b, c shows the reconstructed prior austenite grains in the WZ and TMAZ. The reconstructed prior austenite in the WZ with packs in different colour (see Fig. 12b) appears to have a polygonal microstructure with an average grain size of $\sim 11 \mu\text{m}$. Due to this small size, the formation of packets with HAGB between them inside the prior austenite grains is restricted, which is manifested in the form of lower fraction of HAGB in WZ in the plots of misorientation angle distributions (see Fig. 5). This alternatively implies that in the WZ, each grain is transformed to a single packet. Similar observations on martensitic morphology have been reported elsewhere for different grades of steel [28, 29]. The size of the reconstructed prior austenite grains in the TMAZ (Fig. 12c) varies from 12.4 to 58 μm with the average size being $\sim 29 \mu\text{m}$, larger than those in the WZ; hence the reduction in the fraction of HAGBs compared to the BM was

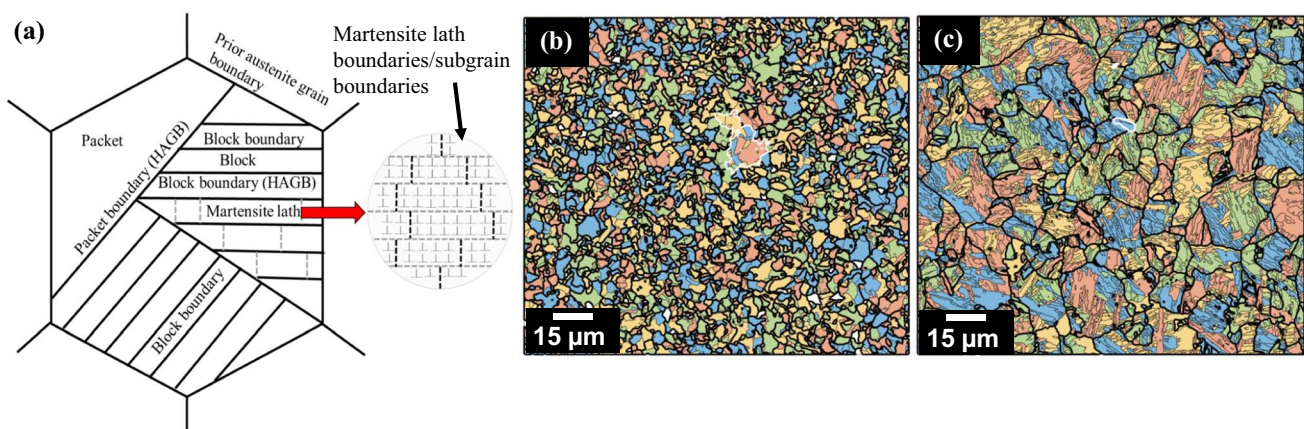


Fig. 12 a Schematic representation of the prior austenite grains and the potential martensite morphologies after austenite \rightarrow martensite transformation, b, c reconstructed prior austenite grains for the WZ and TMAZ, respectively, from the EBSD maps presented in Fig. 4.

The prior austenite grain boundaries are shown in bold black colour. The packets, as well as the lath morphology of bainite and martensite inside the prior austenite grains for the TMAZ, are clearly apparent in c

not as much as that of the WZ. These larger prior austenite grains thus allowed the growth of multiple laths inside the block boundaries (i.e. HAGB); the same has been manifested in the EBSD OIM image (Fig. 4b).

The hardness distribution of the weld zones (see Fig. 6) can be linked to the microstructure distribution throughout the weld cross section shown in Fig. 3. The presence of predominantly martensitic microstructure in the WZ is the primary reason for the higher hardness (i.e. ≈ 3 times) of this region compared to that of the BM. The measured hardness values in the TMAZ are lower than those of the WZ (~ 410 – 510 HV). This drop in the hardness can also be correlated with the microstructure where a lower fraction of martensite was formed in the TMAZ compared to the WZ due to the lower temperature obtained during IFW. The variation in the heat input across the weld cross section (i.e. from outer to inner diameter) is the primary reason for the heterogeneous distribution of temperature during IFW which then results in different microstructure character distribution (e.g. difference in martensite volume fraction in different regions) [31]. The variation in the heat input can also be due to the difference in the angular speed as a function of local diameter across the components during the welding process, such that higher levels of heat is generated at areas with higher angular speed (i.e. closer to the outer diameter).

4.2 Texture development

The evolution of crystallographic texture in different regions of the weld zones have been investigated to understand the likely deformation mechanisms during the IFW process. For this purpose, the originally acquired EBSD maps (Fig. 4), in which the orientations are defined as Euler angles in the specimen reference frame (AD, RD, TD), are rotated to the local shear reference frame (θ , Z , r), using HKL Channel 5 software. The shear direction (\overline{SD} or θ) coincides with the \overline{RD} axis, the shear plane normal (\overline{SPN} or Z) is parallel to the \overline{AD} axis and the rotation axis is aligned with the \overline{TD} axis. The shear components are usually defined by the crystallographic plane $\{hkl\}$ and direction $\langle uvw \rangle$ aligned parallel to the shear plane normal (Z) and shear direction (θ), respectively [12]. In materials with FCC structure, it is the alignment of the $\{111\}$ slip planes with the Z and the $\langle 110 \rangle$ slip direction with θ . The ideal shear texture components for the FCC material are presented in Table 6 [32].

During IFW, the severe shear deformations had occurred at different temperatures, depending on the location within the weld, under compression forces applied from the beginning of the welding process. The results of microstructural analyses by the aid of different techniques, backed up by the microhardness results, suggested that the temperature in the WZ and TMAZ approached temperatures at or above A_{c3} , where the microstructure transforms to fully austenitic with

Table 6 Ideal shear texture components formed during shear deformation in materials with FCC crystal structures, reported by Fonda and Knipling (2011)

Crystal structure	Shear component	$\{hkl\}\langle uvw \rangle$	Euler angles ($^\circ$)		
			Φ_1	Φ	Φ_2
FCC	A_1^*	$\{111\}\langle \bar{1}\bar{1}\bar{2} \rangle$	35.3/215.3	45	0
			125.3/305.3	90	45
	A_2^*	$\{111\}\langle 11\bar{2} \rangle$	144.7/324.7	45	0
			54.7/234.7	90	45
	A	$\{ \bar{1}\bar{1}\bar{1} \}110$	0	35.3	45
	\bar{A}	$\{ \bar{1}\bar{1}\bar{1} \}\bar{1}\bar{1}0$	180	35.3	45
	B	$\{ \bar{1}\bar{1}\bar{2} \}110$	0/120/240	54.7	45
	\bar{B}	$\{ \bar{1}\bar{1}\bar{2} \}\bar{1}\bar{1}0$	60/180/300	54.7	45
	C	$\{001\}110$	90/270	45	0
		0/180	90	45	

FCC crystal structure. Hence, the deformation textures of both the WZ and TMAZ in the reconstructed prior austenite, after rotation to the shear reference frame, are expected to be aligned with the ideal shear deformation components of the FCC material, taking into account that the texture is inherited during the austenite to martensite transformation on cooling [21]. Kurdjumov–Sachs (KS) and Nishiyama–Wasserman (NW) are the well-known methodologies of describing crystallographic orientation relationships (OR) between austenite and martensite, following transformation on cooling. KS crystallographic OR which is used for the reconstruction of prior austenite in this study defines the symmetry between planes and directions in austenite (γ) and martensite (α) such that $\{111\}\gamma//\{110\}\alpha-\langle 110 \rangle\gamma//\langle 111 \rangle\alpha$ [60]. The pole figures for the WZ and TMAZ plotted from the reconstructed austenite, following rotation from the sample reference frame to the expected shear reference frame, are evaluated against the ideal shear texture components for FCC metal and shown in Fig. 13.

Figure 13a, b shows the $\{111\}$ pole figures of the WZ and TMAZ, respectively. The ideal shear texture components for the $\{111\}$ planes of FCC metal in the local shear reference frame are superimposed on these pole figures. There is a reasonably strong match between the C ideal shear texture components of the FCC metal and the measured pole figures for the WZ and TMAZ. B and \bar{B} shear texture components are also present in the WZ and TMAZ, though the intensity does not appear to be as strong (Fig. 13a, b). These observations suggest that the transformed austenite in both the WZ and TMAZ during IFW, undergoes simple shear deformation with negligible effect from the compression forces, and then transformed back to BCC (i.e. martensite, bainite) on

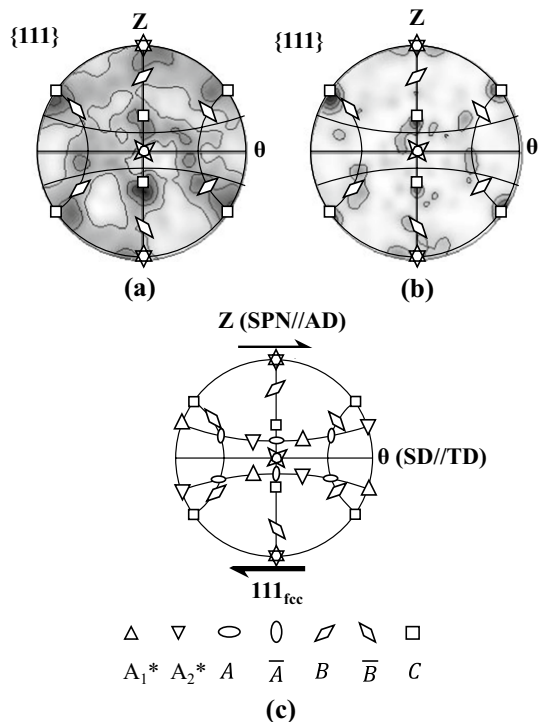


Fig. 13 $\{111\}$ pole figures showing texture in the local shear reference frame of **a**, **b** the WZ and TMAZ, respectively, with the ideal shear deformation components for FCC metals superimposed, after austenite reconstruction, and **c** the ideal shear deformation components for the FCC material

cooling. This further supports the previous observations that during the IFW, when temperature at the WZ and TMAZ was above the A_{c3} temperature, the microstructure was dominated by austenite that was then subjected to shear deformation. A similar explanation and the existence of the dominant B and \bar{B} shear textures in the FCC phase of a pipeline steel (API X80) have also been reported by Abbasi et al. [33].

It is worthwhile to emphasise that during the friction phase of the IFW process, while the shear deformation occurs, the forge (or axial compressive) force is maintained until the end of the initial cooling period to consolidate the weld joint, thereby the rotation of the welded part is stopped. This means that both the shear and compressive deformations are active on the microstructure during the IFW process, which due to temperature gradients contains multiple phases simultaneously such as transformed ferrite, austenite, bainite and martensite. This might lead to combined deformations under both shear and compression in the material, which is manifested in the form of deviation from the ideal texture components in the pole figures (Fig. 13). Comparing these observations with previous studies reported on friction stir welded steels shows that during shear deformation, well-defined ideal shear texture components can result, disregarding the cooling rate and chemical composition [12,

26]. Moreover, the phase transformation phenomenon leads to the formation of thermal stresses during the cooling process, and this may also be considered as a potential reason for the observed deviation in the poles from the ideal shear texture components.

4.3 Mechanical properties of the welds

The measured mechanical properties for the welded materials are strongly dependent on the process parameters used during the IFW process. The existence of the yield point phenomenon (see Fig. 7a) can be attributed to the Cottrell atmosphere effect on the mobile dislocation density. It is well understood that on the commencement of the onset of yielding during mechanical testing, the mobility of the dislocation is restricted by the clustering of solute atoms, such as carbon and nitrogen, which, in turn, leads to the formation of stress concentration sites. Thus, additional stress is required for further movements of these dislocations which results in the upper yield points (or upper yield stress) [34]. Once the material attains the upper yield stress, the dislocations are released from the stress concentration sites. Thus, comparatively lower stress is required for further movement of dislocations and hence a decrease in the stress is observed known as the lower yield point in the stress–strain curve. Note that no double-yielding phenomenon was observed in the tensile test of the as-received material (refer SD). This indicates that the increase in the temperature during IFW resulted in microstructural changes and the diffusion of the interstitial atoms [35]. It was observed that the onset of yielding mostly occurred in the softer areas of the samples, i.e. mainly a region between the HAZ and the BM due to the absence of martensite in these regions.

As observed in Fig. 8b, dual slopes in the strain-hardening behaviour of the welded materials were observed during the tensile experiments. According to Farabi et al. [36], such behaviour is an indication of the formability of the material before the onset of plastic instability begins. This is in agreement with the current findings shown in Fig. 7a, where the highest uniform elongation was obtained for the IW6 condition. Note that the initial peaks in the $\ln \sigma - \ln \epsilon$ curves (see Fig. 8b) are due to the double-yielding phenomena measured for the specimens (see Fig. 7a). The dual slope in the strain-hardening behaviours of the investigated welded materials is due to the difference in the stress experienced by different microstructural phases during the ongoing deformation in tension [35]. The first stage of the strain-hardening behaviour, which corresponds to the upper regime (see Fig. 8b), indicates the deformation in both ferrite and austenite constituents that are softer in nature compared to martensite and bainite. On the other hand, the second stage, which corresponds to the lower regime, represents the deformation of bainite and martensite phases in addition to ferrite

and austenite [23]. These observations are supported by the results of previous studies conducted on the strain-hardening behaviour of dual-phase steels. In general, the carbide precipitates are observed to be only elastically deformed during the entire tensile tests [37]. Therefore, it can be concluded that the carbide precipitates play a significant role in the hardening behaviour of the welded materials.

The decrease in the hardening capacity and strain-hardening exponent values (both n_1 and n_2) of the welded materials, compared to those of the BM, can be linked to the microstructural changes that occurred during the IFW. The presence of different microstructural phases is expected to have a significant effect on the strain-hardening behaviour of the material. Movahed et al. [38] reported a decrease in the strain-hardening exponent value with an increase in the martensite volume fraction in ferritic–martensitic dual-phase steel. It is well understood that increasing ferrite content leads to an upsurge in the dislocations storage capacity and their interactions, which, in turn, results in increasing the hardening capacity of the material. This explains the observed decrease in the hardening capacity and the n values of the welded materials compared to the BM. As evident from Figs. 2 and 3, the BM exhibited a ferritic–bainitic microstructure, whereas the WZ and TMAZ of the welded materials exhibited large fractions of martensite in addition to other phases.

4.4 Effect of IFW process parameters on mechanical properties

The effects of variations in the welding parameters, including the rotational speed of the rotating part, friction force and forging force, on the mechanical behaviour of the material were investigated. To determine the weighing effect of each of these process parameters, an analysis of variance (ANOVA) was carried out as per the standard ANOVA procedure [39]. The ANOVA procedure only evaluates the effect of process parameters on the strength variations individually and the combined effects are neglected. The variation in the signal to noise (S/N) ratio for different process parameters is presented in Fig. 14a and the summarised values are presented in Table 7. The recorded difference of the S/N ratio was very small (≈ 0.2). In these analyses, the F variable provides a confidence level based on the data statistics, whereas the P variable is an indication of the percentage of the total variance of each factor. As shown in Fig. 14a, the forge force and the weld rotational speed have substantial effects on the yield and UTS of the weld due to the higher F ratios. The forge force was found to have a major effect on the weld properties by increasing the tensile strength by $\approx 64\%$ (refer Table 7). The combined effects of forge force and rotational speed on the UTS of the weld are shown in Fig. 14b. The results imply that the UTS of the weld joints

decreases with an increase in the forge force irrespective of the rotational speed. However, a small decrease in the UTS was observed when applying the forge force in the range of 620–660 kN. A similar trend was observed for the yield strength. Meanwhile, the weld strengths (i.e. both yield and UTS) exhibited no specific trends with variations in the friction force. In contrast, an increase in the percentage of elongation was observed with an increase in the friction force. The combined effects of friction force and weld rotational speed on the elongation behaviour of the welded specimens are shown in Fig. 14c. Interestingly, a sharp increase in the percentage of elongation is observed with an upsurge in the friction pressure for the specimens welded under the nominal rotational speed in the range of 2900–3100 rpm.

5 Conclusions

In this paper, the evolution of microstructure, crystallographic texture and mechanical properties in an inertia friction welded AISI 8630 steel have been investigated. The major findings of this study are summarised as follows:

1. The post-IFW microstructural observations showed the formation of microstructure dominated by martensite in the WZ, whereas the presence of ferrite, bainite and carbide precipitates, in addition to martensite, was confirmed in the TMAZ. The HAZ exhibited a similar microstructure to that of the BM. Based on the observed microstructural evolution, it was concluded that the WZ and TMAZ experienced temperatures above Ac_3 . The temperature in the HAZ stayed below Ac_1 and as a result, no drastic microstructure changes occurred during IFW.
2. In the WZ where the microstructure is dominated by austenite during IFW, simple shear was determined as the predominant mode of deformation, whereas the TMAZ, in which the microstructure contains austenite, ferrite and remaining bainite and martensite, the deformation was a combination of shear and compression.
3. The welded materials exhibited a double-yielding phenomenon. In comparison to the BM, all the weld materials exhibited an overall increase in the yield strength decrease in the UTS (except IW6), decrease in the hardening capacity and strain-hardening exponent and almost three times increase in the hardness. Amongst all the weld conditions, the weld produced under the nominal weld rotational speed, maximum friction force and the lowest forge force exhibited the optimum mechanical properties in terms of strength, ductility and static toughness and, therefore, concluded as the best weld condition.

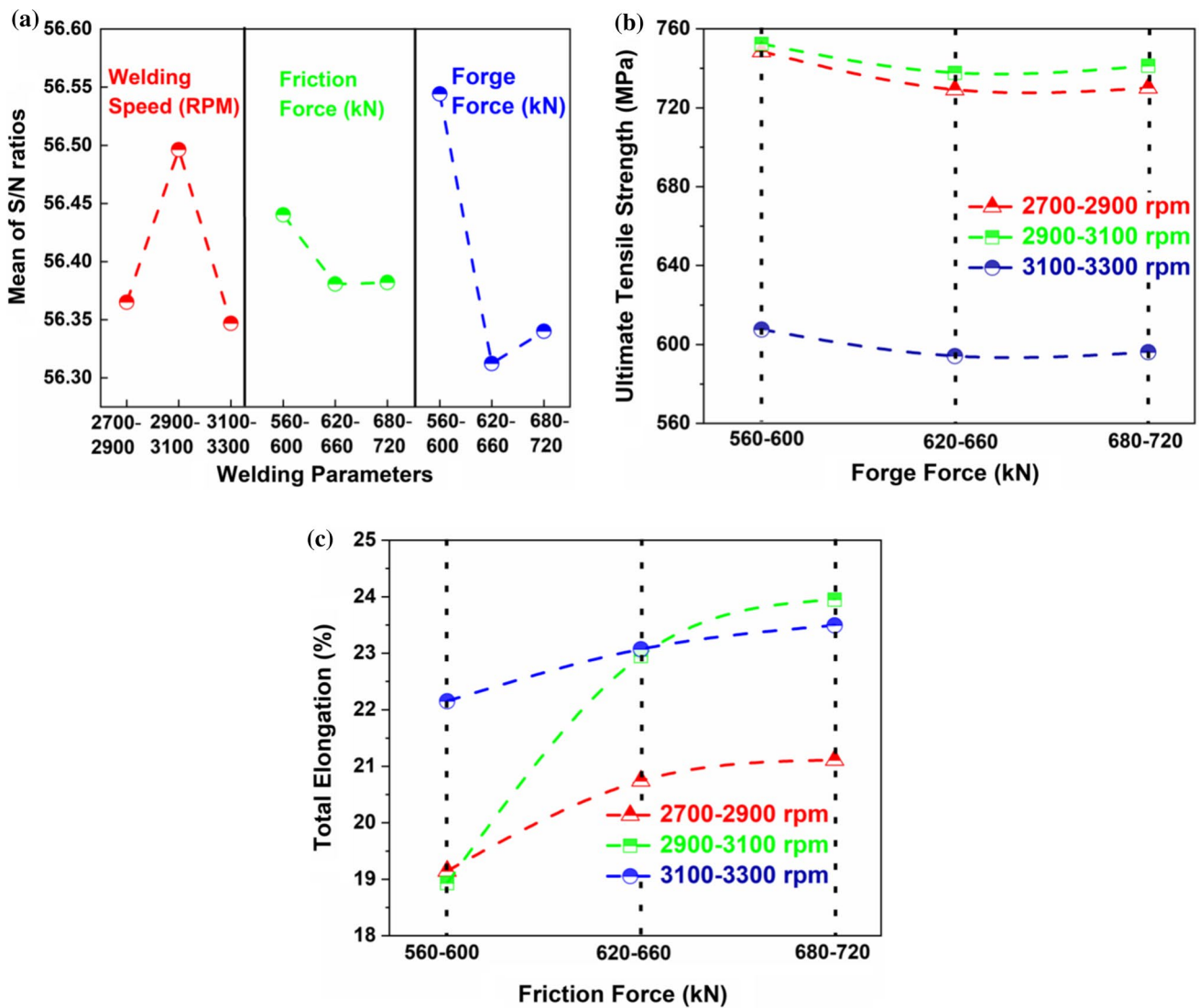


Fig. 14 **a** ANOVA analysis depicting the effect of IFW parameters individually, on the variations in mechanical strengths, **b** combined effects of friction force and rotational speed during IFW on the total percentage of elongation, and **c** combined effects of forge force and rotational speed during IFW on the UTS of the weld

Table 7 Summary of ANOVA analyses for the welded materials

Source	Degree of freedom	Sum of squares	Mean of squares	F test	P test	Contribution (%)
Weld speed	2	207.81	103.90	4.81	0.179	26.70
Friction force	2	30.17	15.08	0.70	0.589	3.87
Forge force	2	496.90	248.45	11.50	0.080	63.86
Residual error	2	43.22	21.61			5.55
Total	8	778.09				100

- The fracture surface of the tensile specimens exhibited the presence of dimples originating from the microvoids along with the presence of transgranular cracks, indicating a ductile mode of failure. The fracture surface of the Charpy V-notch specimens showed protruded shear lips and the formation of dimples.
- The rotational speed and the forge force applied during the IFW were recognised as the major influential param-

eters affecting the mechanical properties of the weld. The combined effects of the weld rotational speed and forge force were found to have a significant effect on the UTS of the material, whereas the combination of weld rotational speed and friction force was found to alter the elongation properties of the welded materials.

Supplementary Information The online version contains supplementary material available at <https://doi.org/10.1007/s43452-021-00300-9>.

Acknowledgements The authors acknowledge the Advanced Forming Research Centre (AFRC), University of Strathclyde for providing the mechanical and material characterisation facilities. The centre received partial financial support from the UK's High-Value Manufacturing CATAPULT. The authors would like to acknowledge Dr. Shanmukh Moturu for his assistance in performing the hardness test, Dr. Anna Florova for OM examination and Kornelia Kondziolka for preparing the metallurgical specimens.

Funding Funding for this study was obtained from the Tier 1 members of the AFRC.

Declarations

Ethical approval This article does not contain any studies with human participants performed by any of the authors.

Open Access This article is licensed under a Creative Commons Attribution 4.0 International License, which permits use, sharing, adaptation, distribution and reproduction in any medium or format, as long as you give appropriate credit to the original author(s) and the source, provide a link to the Creative Commons licence, and indicate if changes were made. The images or other third party material in this article are included in the article's Creative Commons licence, unless indicated otherwise in a credit line to the material. If material is not included in the article's Creative Commons licence and your intended use is not permitted by statutory regulation or exceeds the permitted use, you will need to obtain permission directly from the copyright holder. To view a copy of this licence, visit <http://creativecommons.org/licenses/by/4.0/>.

References

- Sharma SK, Maheshwari S. A review on welding of high strength oil and gas pipeline steels. *J Nat Gas Sci Eng*. 2017;38:203–17.
- Mathias LLS, Sarzosa DFB, Ruggieri C. Effects of specimen geometry and loading mode on crack growth resistance curves of a high-strength pipeline girth weld. *Int J Press Vessels Pip*. 2013;111–112:106–19.
- Banerjee A, Ntovas M, Da Silva L, Rahimi S. Effect of rotational speed and inertia on the mechanical properties and microstructural evolution during inertia friction welding of 8630M steel. *Mater Lett*. 2021;296:129906.
- Kuril AA, Janaki Ram GD, Bakshi SR. Microstructure and mechanical properties of keyhole plasma arc welded dual phase steel DP600. *J Mater Process Technol*. 2019;270:28–36.
- Liu FC, Nelson TW. Grain structure evolution, grain boundary sliding and material flow resistance in friction welding of Alloy 718. *Mater Sci Eng A*. 2018;710:280–8.
- Li W, Vairis A, Preuss M, Ma T. Linear and rotary friction welding review. *Int Mater Rev*. 2016;61(2):71–100.
- Yang LB, Gebelin JC, Reed RC. Modelling of inertia welding of IN718 superalloy. *Mater Sci Technol*. 2011;27(8):1249–64.
- Dey HC, Ashfaq M, Bhaduri AK, Rao KP. Joining of titanium to 304L stainless steel by friction welding. *J Mater Process Technol*. 2009;209(18):5862–70.
- Sathiya P, Aravindan S, Noorul Haq A. Mechanical and metallurgical properties of friction welded AISI 304 austenitic stainless steel. *Int J Adv Manuf Technol*. 2005;26(5):505–11.
- Selvamani ST, Palanikumar K. Optimizing the friction welding parameters to attain maximum tensile strength in AISI 1035 grade carbon steel rods. *Measurement*. 2014;53:10–21.
- Hazra M, Rao KS, Reddy GM. Friction welding of a nickel free high nitrogen steel: influence of forge force on microstructure, mechanical properties and pitting corrosion resistance. *J Market Res*. 2014;3(1):90–100.
- Rahimi S, Konkova TN, Violatos I, Baker TN. Evolution of microstructure and crystallographic texture during dissimilar friction stir welding of duplex stainless steel to low carbon-manganese structural steel. *Metall and Mater Trans A*. 2019;50(2):664–87.
- Rahimi S, Wynne BP, Baker TN. Development of microstructure and crystallographic texture in a double-sided friction stir welded microalloyed steel. *Metall Mater Trans A*. 2017;48(1):362–78.
- Abdul Ghani Khan M, Rajakumar S, Pragatheswaran T. Influence of rotational speed on mechanical and microstructural characteristics on the rotary friction welded as-cast LM25 aluminium alloy. *Mater Today Proc*. 2020
- Daniyan IA, Mpofu K, Adeodu AO. Optimization of welding parameters using Taguchi and response surface methodology for rail car bracket assembly. *Int J Adv Manuf Technol*. 2019;100(9):2221–8.
- Nyyssönen T, Peura P, Kuokkala VT. Crystallography, morphology, and martensite transformation of prior austenite in intercritically annealed high-aluminum steel. *Metall Mater Trans A*. 2018;49(12):6426–41.
- Standard test methods for tension testing of metallic materials [Metric].
- Standard test methods and definitions for mechanical testing of steel products.
- Javaheri V, Khodaie N, Kajjalainen A, Porter D. Effect of niobium and phase transformation temperature on the microstructure and texture of a novel 0.40% C thermomechanically processed steel. *Mater Charact*. 2018;142:295–308.
- Bhadeshia HKDH. Bainite in steels: transformations, microstructure and properties. *IOM Communications*. 2001.
- Zilnyk KD, Oliveira VB, Sandim HRZ, Möslang A, Raabe D. Martensitic transformation in Eurofer-97 and ODS-Eurofer steels: a comparative study. *J Nucl Mater*. 2015;462:360–7.
- Afrin N, Chen DL, Cao X, Jahazi M. Strain hardening behavior of a friction stir welded magnesium alloy. *Scripta Mater*. 2007;57(11):1004–7.
- Banerjee A, Prusty BG, Bhattacharyya S. Rate-dependent mechanical strength and flow behaviour of dual-phase high carbon steel at elevated temperatures: an experimental investigation. *Mater Sci Eng, A*. 2019;744:224–34.
- Wallin K, Karjalainen-Roikonen P, Suikkanen P. Sub-sized CVN specimen conversion methodology. *Proc Struct Integr*. 2016;2:3735–42.
- Mesplont C. Phase transformations and microstructure-mechanical properties relations in complex phase high strength steels. 2002.
- Baker TN, Rahimi S, Wei B, He K, McPherson NA. Evolution of microstructure during double-sided friction stir welding of microalloyed steel. *Metall Mater Trans A*. 2019;50(6):2748–64.

27. Eghbali B, Abdollah-Zadeh A. Deformation-induced ferrite transformation in a low carbon Nb–Ti microalloyed steel. *Mater Des.* 2007;28(3):1021–6.
28. Celada-Casero C, Sietsma J, Santofimia MJ. The role of the austenite grain size in the martensitic transformation in low carbon steels. *Mater Des.* 2019;167:107625.
29. Almeida Junior DR, Zilnyk KD, Raabe D, Sandim HRZ. Reconstructing the austenite parent microstructure of martensitic steels: A case study for reduced-activation Eurofer steels. *J Nucl Mater.* 2019;516:185–93.
30. Kaibyshev R. Microstructural evolution in 9%Cr heat resistant steels under creep conditions. *Mater Sci Forum.* 2012;715–716:813–8.
31. Demouche M, Ouakdi EH, Louahdi R. Effect of welding parameters in the microstructure and mechanical properties of friction-welded joints of 100Cr6 steel. *Iran J Mater Sci Eng.* 2019;16(3):24–31.
32. Fonda RW, Knipling KE. Texture development in friction stir welds. *Sci Technol Weld Join.* 2011;16(4):288–94.
33. Abbasi M, Nelson TW, Sorensen CD. Transformation and deformation texture study in friction stir processed API X80 pipeline steel. *Metall Mater Trans A.* 2012;43(13):4940–6.
34. Mohsenzadeh MS, Mazinani M. On the yield point phenomenon in low-carbon steels with ferrite-cementite microstructure. *Mater Sci Eng, A.* 2016;673:193–203.
35. Dieter GE. *Mechanical metallurgy.* New York: McGraw-Hill; 1986.
36. Farabi N, Chen DL, Zhou Y. Tensile Properties and Work Hardening Behavior of Laser-Welded Dual-Phase Steel Joints. *J Mater Eng Perform.* 2012;21(2):222–30.
37. Wang W, Dong Z, Xu Z, Zhu B, Zhang X, Zhong J, Zhang J. Local strain hardening behavior in a dissimilar metal welded joint with buttering layer of ultra-supercritical turbine rotor. *Mater Sci Eng A.* 2020;785:139379.
38. Movahed P, Kolahgar S, Marashi SPH, Pournavari M, Parvin N. The effect of intercritical heat treatment temperature on the tensile properties and work hardening behavior of ferrite–martensite dual phase steel sheets. *Mater Sci Eng A.* 2009;518(1):1–6.
39. Ross PJ. *Taguchi techniques for quality engineering: loss function, orthogonal experiments, parameter and tolerance design.* New York: McGraw-Hill; 1988.

Publisher's Note Springer Nature remains neutral with regard to jurisdictional claims in published maps and institutional affiliations.